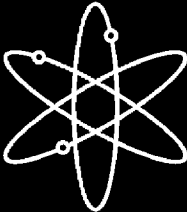


The Battelle Integrity of Nuclear Piping (BINP) Program Final Report

Appendices



**U.S. Nuclear Regulatory Commission
Office of Nuclear Regulatory Research
Washington, DC 20555-0001**



The Battelle Integrity of Nuclear Piping (BINP) Program Final Report

Appendices

Manuscript Completed: September 2003

Date Published: June 2005

Prepared by

P.Scott¹, R.Olson¹, J.Bockbrader¹, M.Wilson¹, B.Gruen¹,
R.Morbitzer¹, Y.Yang¹, C.Williams¹, F.Brust¹, L.Fredette¹,
N.Ghadiali¹

G.Wilkowski², D.Rudland², Z.Feng², R.Wolterman²

¹Battelle

505 King Avenue
Columbus, OH 43201

Subcontractor:

²Engineering Mechanics Corporation of Columbus
3518 Riverside Drive
Suite 202
Columbus, OH 43221-1735

C. Greene, NRC Project Manager

Prepared for
Division of Engineering Technology
Office of Nuclear Regulatory Research
U.S. Nuclear Regulatory Commission
Washington, DC 20555-0001
NRC Job Code W6775



**AVAILABILITY OF REFERENCE MATERIALS
IN NRC PUBLICATIONS**

NRC Reference Material

As of November 1999, you may electronically access NUREG-series publications and other NRC records at NRC's Public Electronic Reading Room at <http://www.nrc.gov/reading-rm.html>. Publicly released records include, to name a few, NUREG-series publications; *Federal Register* notices; applicant, licensee, and vendor documents and correspondence; NRC correspondence and internal memoranda; bulletins and information notices; inspection and investigative reports; licensee event reports; and Commission papers and their attachments.

NRC publications in the NUREG series, NRC regulations, and *Title 10, Energy*, in the Code of *Federal Regulations* may also be purchased from one of these two sources.

1. The Superintendent of Documents
U.S. Government Printing Office
Mail Stop SSOP
Washington, DC 20402-0001
Internet: bookstore.gpo.gov
Telephone: 202-512-1800
Fax: 202-512-2250
2. The National Technical Information Service
Springfield, VA 22161-0002
www.ntis.gov
1-800-553-6847 or, locally, 703-605-6000

A single copy of each NRC draft report for comment is available free, to the extent of supply, upon written request as follows:

Address: Office of the Chief Information Officer,
Reproduction and Distribution
Services Section
U.S. Nuclear Regulatory Commission
Washington, DC 20555-0001
E-mail: DISTRIBUTION@nrc.gov
Facsimile: 301-415-2289

Some publications in the NUREG series that are posted at NRC's Web site address <http://www.nrc.gov/reading-rm/doc-collections/nuregs> are updated periodically and may differ from the last printed version. Although references to material found on a Web site bear the date the material was accessed, the material available on the date cited may subsequently be removed from the site.

Non-NRC Reference Material

Documents available from public and special technical libraries include all open literature items, such as books, journal articles, and transactions, *Federal Register* notices, Federal and State legislation, and congressional reports. Such documents as theses, dissertations, foreign reports and translations, and non-NRC conference proceedings may be purchased from their sponsoring organization.

Copies of industry codes and standards used in a substantive manner in the NRC regulatory process are maintained at—

The NRC Technical Library
Two White Flint North
11545 Rockville Pike
Rockville, MD 20852-2738

These standards are available in the library for reference use by the public. Codes and standards are usually copyrighted and may be purchased from the originating organization or, if they are American National Standards, from—

American National Standards Institute
11 West 42nd Street
New York, NY 10036-8002
www.ansi.org
212-642-4900

Legally binding regulatory requirements are stated only in laws; NRC regulations; licenses, including technical specifications; or orders, not in NUREG-series publications. The views expressed in contractor-prepared publications in this series are not necessarily those of the NRC.

The NUREG series comprises (1) technical and administrative reports and books prepared by the staff or agency contractors, (2) proceedings of conferences, (3) reports resulting from international agreements, (4) brochures, and (5) compilations of legal decisions and orders of the Commission and Atomic and Safety Licensing Boards and of Directors' decisions under Section 2.206 of NRC's regulations (NUREG-0750).

DISCLAIMER: This report was prepared as an account of work sponsored by an agency of the U.S. Government. Neither the U.S. Government nor any agency thereof, nor any employee, makes any warranty, expressed or implied, or assumes any legal liability or responsibility for any third party's use, or the results of such use, of any information, apparatus, product, or process disclosed in this publication, or represents that its use by such third party would not infringe privately owned rights.

ABSTRACT

Volume I of the final report for the Battelle Integrity of Nuclear Piping (BINP) program provided a summary of the results from this program and a discussion of the implications of those results. This volume (Volume II - Appendices) provides the details from

the various technical tasks conducted as part of this program. Each individual appendix provides the details of a specific task conducted as part of the BINP program.

FOREWORD

Since 1965, the U.S. Nuclear Regulatory Commission (NRC) has been involved in research on various aspects of pipe fracture in nuclear power plant piping systems. The most recent programs are the Degraded Piping Program, Short Cracks in Piping and Piping Welds Program, and two International Piping Integrity Research Group programs. These programs have developed and validated “state-of-the-art” structural analysis methods and data for nuclear piping systems.

This report describes the results of the Battelle Integrity of Nuclear Piping (BINP) program, which was performed by Battelle Columbus Laboratories. The objective of the BINP program was to address the most important unresolved technical issues from the earlier research programs. The BINP program was initiated as an international program to enable fiscal leveraging and an expanded scope of work. Technical direction for the program was provided by a Technical Advisory Group composed of representatives from the funding organizations.

The BINP program was divided into eight independent tasks, each of which examined one of the unresolved technical issues. These eight tasks included both experimental and analytical efforts. The two pipe-system experiments examined the effects of secondary stresses (such as thermal expansion) and cyclic loading (such

as during a seismic event) on the load-carrying capacity of flawed piping. For these experiments, the pipe system had large flaws or cracks. The remaining six tasks were “best-estimate” analyses to examine the effects of other factors, such as pipe system boundary conditions, and weld residual stresses on the behavior of flawed pipes. Many of these analyses involved the use of finite element modeling techniques. One of these analytical tasks was to examine the actual margins that may exist in flawed pipe evaluations as a result of non-linear behavior. While the magnitude of these margins would vary on a case-by-case basis, the results of this task show that a potential for significant margins does exist.

In addition to developing a technical basis for more advanced inservice flaw evaluation procedures for use with Class 1 piping, as defined by the American Society of Mechanical Engineers (ASME), the BINP program considered the development of flaw evaluation procedures for ASME Class 2 and 3 piping and balance-of-plant piping.

This research supports the NRC’s goal to improve the effectiveness and realism of the agency’s regulatory actions.

Carl Paperiello, Director
Office of Nuclear Regulatory Research
U.S. Nuclear Regulatory Commission

Table of Contents

Abstract.....	iii
Foreword.....	v
Appendix A Evaluation of Procedures for the Treatment of Secondary Stresses in Pipe Fracture Analyses.....	A1
Appendix B Pipe-System Experiment with an Alternative Simulated Seismic Load History.....	B1
Appendix C BINP Task 3 – Determination of Actual Margins in Plant Piping.....	C1
Appendix D Analytical Expressions Incorporating Restraint of Pressure-Induced Bending in Crack-Opening Displacement Calculations.....	D1
Appendix E Development of Flaw Evaluation Criteria for Class 2, 3, and Balance of Plant Piping.....	E1
Appendix F The Development of a J-Estimation Scheme for Circumferential and Axial Through-Wall Cracked Elbows.....	F1
Appendix G Evaluation of Reactor Pressure Vessel (RPV) Nozzle to Hot-Leg Piping Bimetallic Weld Joint Integrity for the V. C. Summer Nuclear Power Plant.....	G1
Appendix H The Effect of Weld Induced Residual Stresses on Pipe Crack Opening Areas and Implications on Leak-Before-Break Considerations.....	H1
Appendix I Round Robin Analyses.....	I1

List of Figures

Figure A.1 Comparison of the results from the IPIRG-1 pipe-system experiments with companion quasi-static, four-point bend experiments demonstrating how global secondary stresses, such as thermal expansion and seismic anchor motion stresses, contribute to fracture.....	A2
Figure A.2 Actuator time history for BINP Task 1 experiment and IPIRG-1 Experiment 1.3-5	A3
Figure A.3 Plot of crack section moment as function of time for BINP Task 1 experiment and IPIRG-1 Experiment 1.3-5	A4
Figure A.4 Comparison of the results from four stainless steel weld experiments showing the contributions of the various stress components to pipe fracture.....	A4

Figure B.1 Actuator displacement-time history for IPIRG-2 simulated seismic forcing function for stainless steel base metal experiment (Experiment 1-1).....	B2
Figure B.2 Moment-rotation response for IPIRG-2 simulated seismic forcing function for stainless steel base metal experiment (Experiment 1-1).....	B2
Figure B.3 Traditional seismic design process	B4
Figure B.4 Hypothesized worst case seismic loading.....	B6
Figure B.5 Typical SSE seismic floor-response spectra.....	B6
Figure B.6 Fracture toughness properties from pipe DP2-A8i.....	B7
Figure B.7 Fracture toughness properties from pipe DP2-A8ii.....	B7
Figure B.8 Spring-slider model for a surface crack.....	B8
Figure B.9 Kinematic hardening assumption under unloading conditions.....	B9
Figure B.10 The effect of pressure on crack moment-rotation behavior (BINP Task 2 flaw, A8ii-20 dynamic monotonic J-resistance).....	B9
Figure B.11 Crack unloading behavior.....	B10
Figure B.12 IPIRG-2 Experiment 1-1 cracked-section moment-rotation response.....	B12
Figure B.13 IPIRG-2 Experiment 1-1 cracked-section moment-time history.....	B12
Figure B.14 IPIRG-2 Experiment 1-1 predicted cracked-section upper envelop moment-rotation from the SC.TNP1 J-estimation scheme.....	B13
Figure B.15 Predicted IPIRG-2 Experiment 1-1 moment-rotation history using the dynamic $R = -0.3$ J-R curve with the new asymmetric moment-rotation model	B13
Figure B.16 Predicted IPIRG-2 Experiment 1-1 moment-time history with the dynamic $R = -0.3$ J-R curve with the new asymmetric moment-rotation model.....	B14
Figure B.17 Predicted IPIRG-2 Experiment 1-1 moment-rotation history with the dynamic $R = -1.0$ J-R curve with the new asymmetric moment-rotation model	B14
Figure B.18 Predicted IPIRG-2 Experiment 1-1 moment-time history with the dynamic $R = -1.0$ J-R curve with the new asymmetric moment-rotation model.....	B15
Figure B.19 Old (1993) IPIRG-2 Experiment 1-1 pretest design analysis moment-rotation history results.....	B15
Figure B.20 Old (1993) IPIRG-2 Experiment 1-1 pretest design analysis moment-time results.....	B16
Figure B.21 The IPIRG-2 Round-Robin Problem C.1 floor-response spectrum (IPIRG-2 simulated-seismic forcing function actuator acceleration at SSE loading).....	B18
Figure B.22 IPIRG-2 Round-Robin Problem C.1 predicted linear moment response from Solution F-3a	B18
Figure B.23 IPIRG-2 Round-Robin Problem C.1 predicted linear moment response from Solution D.....	B19

Figure B.24 IPIRG-2 Round-Robin Problem C.1 Solution F-3a actuator displacement forcing function.....	B19
Figure B.25 IPIRG-2 Round-Robin Problem C.1 Solution D actuator displacement forcing function.....	B20
Figure B.26 BINP Task 2 predicted cracked-section upper envelop moment-rotation from the SC.TNP1 J-estimation scheme	B21
Figure B.27 Predicted BINP Task 2 cracked-section moment-rotation behavior using the dynamic $R = -0.3$ J-R curve.....	B22
Figure B.28 Predicted BINP Task 2 moment-time behavior using the dynamic $R = -0.3$ J-R curve	B23
Figure B.29 Predicted BINP Task 2 cracked-section moment-rotation behavior using the quasi-static $R = -0.3$ J-R curve	B23
Figure B.30 Predicted BINP Task 2 moment-time behavior using the quasi-static $R = -0.3$ J-R curve	B24
Figure B.31 The BINP simulated-seismic forcing function actuator displacement	B24
Figure B.32 The IPIRG-2 simulated-seismic forcing function actuator displacement at 3 SSE	B25
Figure B.33 Actuator displacement-time history for BINP Task 2 experiment	B26
Figure B.34 Crack section moment-time response for BINP Task 2 experiment	B27
Figure B.35 Crack section moment-CMOD response for BINP Task 2 experiment.....	B27
Figure B.36 Actuator displacement-time history for IPIRG-1 Experiment 1.3-3	B29
Figure B.37 Crack section moment-rotation response for IPIRG-1 Experiment 1.3-3	B29
Figure B.38 Comparison of J-R curves for two heats of DP2-A8 stainless steel	B30
Figure B.39 Ratio of quasi-static cyclic J values to J for quasi-static monotonic loading as a function of crack growth () a)	B31
Figure B.40 Predicted moment-rotation behavior for 16-inch diameter schedule 100 stainless steel pipe for quasi-static monotonic and quasi-static cyclic ($R = -1$) J-R curves.....	B32
Figure B.41 Predicted moment-rotation behavior for 32-inch diameter carbon steel pipe for quasi-static monotonic and quasi-static cyclic ($R = -1$) J-R curves	B32
Figure C.1 New Production Reactor moment-time history from both a linear and nonlinear analysis: a large margin exists between these two analyses.....	C2
Figure C.2 Plasticity validation bend geometry nomenclature.....	C4
Figure C.3 Plasticity validation pipe cross-section nomenclature.....	C6
Figure C.4 Spring-slider model for a surface crack (or a through-wall crack).....	C12
Figure C.5 Kinematic hardening assumption under unloading conditions.....	C12

Figure C.6 The effect of pressure on crack moment-rotation behavior (BINP Task 2 flaw, A8ii-20 dynamic monotonic J-resistance)	C13
Figure C.7 Crack unloading behavior	C14
Figure C.8 IPIRG-2 Experiment 1-1 cracked-section moment-rotation response.....	C16
Figure C.9 IPIRG-2 Experiment 1-1 cracked-section moment-time history	C16
Figure C.10 IPIRG-2 Experiment 1-1 predicted cracked-section upper envelop moment-rotation from the SC.TNP1 J-estimation scheme.....	C17
Figure C.11 Predicted IPIRG-2 Experiment 1-1 moment-rotation history using the dynamic R=-0.3 J-R curve with the new asymmetric moment-rotation model	C17
Figure C.12 Predicted IPIRG-2 Experiment 1-1 moment-time history with the dynamic R=-0.3 J-R curve with the new asymmetric moment-rotation model.....	C18
Figure C.13 Predicted IPIRG-2 Experiment 1-1 moment-time history with the dynamic R=-1.0 J-R curve with the new asymmetric moment-rotation model.....	C18
Figure C.14 Predicted IPIRG-2 Experiment 1-1 moment-time history with the dynamic R=-1.0 J-R curve with the new asymmetric moment-rotation model.....	C19
Figure C.15 Old (1993) IPIRG-2 Experiment 1-1 pretest design analysis moment-rotation history results.....	C19
Figure C.16 Old (1993) IPIRG-2 Experiment 1-1 pretest design analysis moment-time results.....	C20
Figure C.17 PWR model surge line with global reference axes.....	C21
Figure C.18 Side view of the surge line.....	C21
Figure C.19 Top view of the surge line	C22
Figure C.20 Front view of the surge line	C22
Figure C.21 View looking down the surge line, more or less along the #30 local coordinate system X axis.....	C24
Figure C.22 Top view of the surge line showing local coordinate system #30.....	C24
Figure C.23 View looking down the surge line, more or less along the rotated #30 local coordinate system X axis.....	C25
Figure C.24 Artist's rendition of the IPIRG pipe test facility.....	C26
Figure C.25 Dimensions of the IPIRG pipe loop.....	C27
Figure C.26 Actual Margins forcing function used for IPIRG pipe loop analyses.....	C29
Figure C.27 IPIRG pipe system reference moments	C31
Figure C.28 IPIRG pipe system large surface crack results	C31
Figure C.29 IPIRG pipe system small surface crack results.....	C32
Figure C.30 IPIRG pipe system large through-wall crack results	C32
Figure C.31 IPIRG pipe system small through-wall crack results.....	C33

Figure C.32 PWR system model piping	C35
Figure C.33 PWR System Model Reactor	C35
Figure C.34 PWR system model primary loop (one of three)	C36
Figure C.35 PWR plant model stream generator and coolant pump support	C36
Figure C.36 PWR plant model surge line and pressurizer	C37
Figure C.37 PWR system model safety injection system (SIS) line.....	C37
Figure C.38 PWR system model piping	C38
Figure C.39 PWR system model containment building internal concrete.....	C38
Figure C.40 PWR system model containment.....	C39
Figure C.41 PWR model X-axis loading.....	C40
Figure C.42 PWR model Y-axis loading.....	C40
Figure C.43 Beaver Valley PWR artificial time history horizontal SSE (Ref. C.16).....	C41
Figure C.44 PWR primary piping margin evaluation locations, 1 of 2	C43
Figure C.45 PWR primary piping margin evaluation locations, 2 of 2	C43
Figure C.46 PWR surge line margin evaluation locations.....	C44
Figure C.47 Safety injection system line margin evaluation locations.....	C44
Figure C.48 Margins from the PWR hot leg locations	C45
Figure C.49 Margins from the PWR cross-over leg locations.....	C45
Figure C.50 Margins from the PWR cold leg locations.....	C46
Figure C.51 Margins from the PWR surge line locations.....	C46
Figure C.52 Margins from the PWR safety injection system line locations.....	C47
Figure D.1 Rotation of unrestraint pipe due to pressure induced bending. The rotation of the pipe is magnified by factor of 2.....	D1
Figure D.2 Reduction of COD in pressure-induced-bending of a restrained pipe. An asymmetric pipe restraint condition is shown. Displacement magnified by a factor of 5.	D1
Figure D.3 Cracked-pipe geometry.....	D3
Figure D.4 Loading and boundary conditions of a symmetrically restrained pipe.....	D4
Figure D.5 Beam model representing deformation of cracked pipe under restraint (Ref. D.5).....	D6
Figure D.6 Normalized COD for different pipe diameters (Ref. D.4).....	D6
Figure D.7 Comparison of the $I_b(\theta)$ values for different curve-fitting coefficients.....	D7
Figure D.8 Comparison of the normalizing factor between the analytical expression and the FE calculations. Symmetric restraint, $R_m/t=5$	D7

Figure D.9 Comparison of the normalizing factor between the analytical expression and the FE calculations. The FE results from different round-robin participants are indicated by different letters. Symmetric restraint, $R_m/t=10$	D8
Figure D.10 Comparison of the normalizing factor between the analytical expression and the FE calculations. Symmetric restraint, $R_m/t=20$	D8
Figure D.11 Comparison of the normalizing factor between analytical expression and the FE calculations. Symmetric restraint, $R_m/t=40$	D9
Figure D.12 Comparison of the normalizing factor between the analytical expression and the FE calculations. Symmetric restraint, $R_m/t=40$. NUREG/CR-4572 curve-fitting of coefficients of A_b , B_b , and C_b	D9
Figure D.13 Comparison of Miura's analytical solution with FE results for asymmetric restraint cases. Letters indicate the FE results from different round-robin participants. $R_m/t=10$, $\theta=\pi/2$	D10
Figure D.14 Equivalent normalized restraint length as function of the ratio of L_{R2}/L_{R1}	D11
Figure D.15 PIB of a cracked pipe with one-sided restraint. $\theta=\pi/2$, $R_m/t=10$, $L_{R1}/D_m=1$, $L_{R2}/D_m \rightarrow \infty$	D12
Figure D.16 General form of the correction function.....	D13
Figure D.17 Reference restraint length as function of crack size ($R_m/t=10$).....	D13
Figure D.18 Verification of analytical expression for asymmetric restraint cases ($R_m/t=10$, $\theta=\pi/8$).....	D13
Figure D.19 Verification of analytical expression for asymmetric restraint cases ($R_m/t=10$, $\theta=\pi/4$).....	D14
Figure D.20 Verification of analytical expression for asymmetric restraint cases ($R_m/t=10$, $\theta=\pi/2$).....	D14
Figure D.21 Moment about a hinge; bends and various supports affect the restraint lengths of the pipe about the hinge.....	D15
Figure D.22 Schematic of ANSYS pipe model used to determine stiffness values given various restraint lengths.....	D16
Figure D.23 Plot of restraint length in terms of stiffness for symmetric Case 1; k and L_R/D_m are related by a power function multiplied by a constant.....	D17
Figure D.24 Plot of constant C in terms of second moment of area I for all symmetric cases (The second moment of area is linearly related to the constant C).....	D17
Figure D.25 Comparison of normalizing factors for parametric and stiffness-based L_R/D_m values in cases of symmetric restraint.....	D19
Figure D.26 Plot of restraint length in terms of stiffness for asymmetric Case 1.a.....	D19
Figure D.27 Comparison of normalizing factor between parametric and stiffness-based values of L_R/D_m for asymmetric restraint.....	D20
Figure D.28 Critical flaw locations in the hot and cold legs.....	D20

Figure D.29 Critical flaw locations in the crossover leg	D21
Figure D.30 Critical flaw locations in the surge line	D21
Figure D.31 Critical flaw locations in the safety injection system	D22
Figure E.1 Comparison of best-fit curve-fit expressions for F with numerical results from finite element analyses as a function of R/t ratio for various crack lengths for a constant crack depth of a/t = 0.4.....	E3
Figure E.2 Comparison of best-fit curve-fit expressions for F with numerical results from finite element analyses as a function of crack length for various R/t ratios for a constant crack depth of a/t = 0.4.....	E4
Figure E.3 Comparison of best-fit curve-fit expressions for F with numerical results from finite element analyses as a function of crack depth for various crack lengths for a constant R/t ratio of 20.....	E4
Figure E.4 Differences in J-estimation scheme predictions for same diameter pipe with crack dimensions of $\theta/\pi = 0.5$, $a/t = 0.5$ and $n = 5$	E7
Figure E.5 A typical model using shell and line-spring elements	E11
Figure E.6 Focused view of the shell and line-spring model, looking at the cross-sectional plane containing the line-spring elements.....	E11
Figure E.7 A deformed shell and line-spring model.....	E13
Figure E.8 Axial stress contours of a deformed shell and line-spring model.....	E13
Figure E.9 J versus moment from finite element analyses for $R_m/t = 5$ and all a/t and θ/π values investigated. (Top) no internal pressure (Bottom) internal pressure (Notation: rt05→ $R_m/t = 5$, at25→ a/t = 0.25, cc25→ $\theta/\pi = 0.25$, p→pressure).....	E14
Figure E.10 J versus moment from finite element analyses for $R_m/t = 20$ and all a/t and θ/π values investigated. (Top) no internal pressure (Bottom) internal pressure (Notation: rt20→ $R_m/t = 20$, at25→ a/t = 0.25, cc25→ $\theta/\pi = 0.25$, p→pressure).....	E15
Figure E.11 J versus moment from finite element analyses for $R_m/t = 40$ and all a/t and θ/π values investigated. (Top) no internal pressure (Bottom) internal pressure (Notation: rt40→ $R_m/t = 40$, at25→ a/t = 0.25, cc25→ $\theta/\pi = 0.25$, p→pressure).....	E16
Figure E.12 J versus moment from finite element analyses for $R_m/t = 60$ and all a/t and θ/π values investigated. (Top) no internal pressure (Bottom) internal pressure (Notation: rt60→ $R_m/t = 60$, at25→ a/t = 0.25, cc25→ $\theta/\pi = 0.25$, p→pressure).....	E17
Figure E.13a J versus moment from FEA and NRCPIPES J-estimation schemes for $R_m/t = 5$, a/t= 0.5 and $2\mathbf{B} = 0.25$	E19
Figure E.13b J versus moment from FEA and NRCPIPES J-estimation schemes for $R_m/t = 20$, a/t = 0.5, and $2\mathbf{B} = 0.25$	E19
Figure E.13c J versus moment from FEA and NRCPIPES J-estimation schemes for $R_m/t = 40$, a/t= 0.5 and $2\mathbf{B} = 0.25$	E20

Figure E.14 J versus moment from FEA (symbol) and the SC.TNP1 analysis in NRCPIPES (symbol and line) for $R_m/t = 5$ and all a/t and θ/π values investigated. (Top) no internal pressure (Bottom) internal pressure (Notation as previously described)	E21
Figure E.15 J versus moment from FEA (symbol) and the SC.TNP1 analysis in NRCPIPES (symbol and line) for $R_m/t = 20$ and all a/t and θ/π values investigated. (Top) no internal pressure (Bottom) internal pressure (Notation as previously described)	E22
Figure E.16 J versus moment from FEA (symbol) and the SC.TNP1 analysis in NRCPIPES (symbol and line) for $R_m/t = 40$ and all a/t and θ/π values investigated. (Top) no internal pressure (Bottom) internal pressure (Notation as previously described)	E23
Figure E.17 J versus moment from FEA (symbol) and the SC.TNP1 analysis in NRCPIPES (symbol and line) for $R_m/t = 60$ and all a/t and θ/π values investigated. (Top) no internal pressure (Bottom) internal pressure (Notation as previously described)	E24
Figure E.18 Length correction coefficient (C_1) as a function of R_m/t and a/t for $\theta/\pi = 0.25$ and no internal pressure.....	E25
Figure E.19 Length correction coefficient (C_1) as a function of R_m/t and a/t for $\theta/\pi = 0.50$ and no internal pressure.....	E26
Figure E.20 Length correction coefficient (C_1) as a function of R_m/t and a/t for $\theta/\pi = 0.25$ with internal pressure applied to produce a longitudinal stress equivalent to $S_m/2$	E26
Figure E.21 Length correction coefficient (C_1) as a function of R_m/t and a/t for $\theta/\pi = 0.50$ with internal pressure applied to produce a longitudinal stress equivalent to $S_m/2$	E27
Figure E.22 J versus moment as a function on strain-hardening exponent (n).....	E28
Figure E.23 C_1 versus strain hardening exponent (n) relationship.....	E28
Figure E.24 Comparison of J versus moment response between the revised SC.TNP analysis ($L_w = C_1 * t$) and FEA analysis for the case of $a/t = 0.5$, $2B = 0.25$, no pressure, and $R/t = 5$	E30
Figure E.25 Comparison of J versus moment response between the revised SC.TNP analysis ($L_w = C_1 * t$) and FEA analysis for the case of $a/t = 0.5$, $2B = 0.25$, no pressure, and $R/t = 20$	E30
Figure E.26 Comparison of J versus moment response between the revised SC.TNP analysis ($L_w = C_1 * t$) and FEA analysis for the case of $a/t = 0.5$, $2B = 0.25$, no pressure, and $R/t = 40$	E31
Figure E.27 Comparison of J versus moment response between the revised SC.TNP analysis ($L_w = C_1 * t$) and FEA analysis for the case of $a/t = 0.5$, $2B = 0.25$, no pressure, and $R/t = 60$	E31
Figure E.28 Comparison of J versus moment response between the revised SC.TNP analysis ($L_w = C_1 * t$) and FEA analysis for the case of $a/t = 0.25$, $2B = 0.50$, pressure = 3.055 MPa, and $R/t = 40$	E32
Figure E.29 Plot of the ratio of the experimental stress to the predicted stress as a function of pipe R/t ratio for pipes expected to fail under limit-load conditions.....	E33

Figure E.30 Photo showing a Charpy and full-thickness DWTT specimens on a pipe.....	E37
Figure E.31 Comparison of fracture appearances (percentage of shear area on the fracture) from full-scale dynamic crack propagation results to impact results from the DWTT.....	E37
Figure E.32 Results showing the transition curve differences between a 2/3-thickness Charpy specimen and DWTT specimens of different thicknesses from the same material.....	E38
Figure E.33 Experimental results from several investigators showing the effect of thickness on the difference between the Charpy and DWTT 85% SATT, Ref. E.16	E38
Figure E.34 Axial through-wall-cracked pipe and DWTT data showing the temperature shift from the FITT to the FPTT for linepipe steel – Case 1, Ref. E.17	E39
Figure E.35 Axial through-wall-cracked pipe and DWTT data showing the temperature shift from the FITT _(TWC) to the FPTT for linepipe steel – Case 2, Ref. E.17	E39
Figure E.36 Comparison of $t \times 2t$ CTOD transition temperature with axial through-wall-cracked 48-inch (1,219-mm) diameter pipe fracture data, Ref. E.18.....	E41
Figure E.37 Results from Kiefner showing surface-flawed pipe results relative to FPTT from DWTT data, Ref. E.17.....	E41
Figure E.38 Results from Sugie showing surface-flawed pipe results relative to bend-bar FITT, Ref. E.19	E42
Figure E.39 Fixed-grip SEN(T) specimen (Side-grooves in photo not illustrated in sketch)...	E42
Figure E.40 Results from Ref. E.20 in comparing transition temperatures of bend-bar specimens and fixed-grip SEN(T) specimen.....	E43
Figure E.41 Charpy energy curves for A106B – WRC Bulletin 175 (Ref. E.22) (Orientation D is for circumferential surface flaw Orientation A is for axial through-wall flaw – typically reported).....	E45
Figure E.42 Normalized fit of Charpy shear area transition curves from lower-strength linepipe steels (Ref. E.15)	E45
Figure E.43 Relationship between DWTT and Charpy 85% shear area transition temperatures (SATT) as function of Charpy specimen thickness (Ref. E.15).....	E46
Figure E.44 Shear area versus temperature from full-thickness Charpy test data for A106B taken from PIFRAC database, Ref. E.23	E47
Figure E.45 Preliminary FITT relationship as a function of material thickness and crack depth (Based on upper-bound A106B data in PIFRAC database – L-C orientation)	E50
Figure E.46 Charpy data from PIFRAC for A516 Grade 70 pipe and welds	E53
Figure E.47 Charpy data from PIFRAC for one A106B pipe weld.....	E53
Figure E.48 Shear area as a function of test temperature for the Charpy specimen tests for material DP2-F93 and F94	E54
Figure E.49 Shear area as a function of test temperature for the DTT specimen tests for material DP2-F93 and F94.....	E55
Figure E.50 Load versus displacement records for compact (tension) tests.....	E56

Figure E.51	Load versus actuator displacement data for the SEN(T) specimens.....	E57
Figure E.52	Ductile crack growth as a function of temperature for the SEN(T) specimens	E57
Figure E.53	Crack geometry for the surface-cracked pipe experiments.....	E58
Figure E.54	Loading fixture used in the surface-cracked pipe experiments.....	E58
Figure E.55	Cooling apparatus used in the surface-cracked pipe experiments	E59
Figure E.56	Load versus displacement records for the three surface-cracked pipe experiments.....	E60
Figure E.57	Plot of the ratio of the maximum experiment moment normalized by the Net-Section-Collapse moment (M_{max}/M_{NSC}) as a function of the test temperatures for the three surface-cracked pipe experiments	E60
Figure F.1	Crack geometries considered for elbows	F3
Figure F.2	Typical finite element mesh and model geometry for (a) a 90-degree circumferential crack and (b) a 15-degree axial flank crack.....	F4
Figure F.3	Typical mesh (circumferential crack, 45-degree crack) (a) one element through thickness and (b) four elements through thickness.....	F5
Figure F.4	Illustration of ovalization effects on stresses near the crack tip (Numbers represent crack opening stresses normalized with yield strength)	F7
Figure F.5	Summary of ovalization effects on crack opening response of circumferential cracks in elbows subjected to bending.....	F8
Figure F.6	Illustration of ovalization effects for 15-degree axial flank crack	F9
Figure F.7	Crack opening plots for axially cracked elbows – bending	F11
Figure F.8	Crack opening profile for axial cracks	F13
Figure F.9	Convergence of h-functions versus applied load	F16
Figure F.10	Convergence of h-functions versus lambda	F17
Figure F.11	Comparison between Ramberg-Osgood relationship and typical flow theory representation.....	F17
Figure F.12	Validation check ($R/t = 20$, axial crack $2\theta = 15$ degrees, $n = 5$)	F18
Figure F.13	Validation check ($R/t = 5$, axial crack, $2\theta = 15$ degrees, $n = 5$)	F19
Figure F.14	Validation check ($R/t = 5$, axial crack, $2\theta = 30$ degrees, $n = 5$)	F20
Figure F.15	Validation check ($R/t = 5$ circumferential crack, $2\theta = 90$ degrees, $n=5$).....	F21
Figure F.16	Validation check ($R/t = 20$, circumferential crack, $2\theta = 90$ degrees, $n = 5$).....	F22
Figure F.17	Validation check ($R/t = 20$, circumferential crack, $2\theta = 180$ degrees, $n = 5$).....	F23
Figure F.18	Comparison of J versus moment curves for a circumferential through-wall crack in a straight pipe and centered on the extrados of an elbow with an $R/t = 20$ and $2\theta=90$ degrees.....	F38

Figure F.19 Comparison of J versus moment curves for a circumferential through-wall crack in a straight pipe and centered on the extrados of an elbow with an $R/t = 20$ and $2\theta=180$ degrees.....	F38
Figure F.20 Comparison of J versus moment curves for a circumferential through-wall crack in a straight pipe and centered on the extrados of an elbow with an $R/t = 5$ and $2\theta=90$ degrees.....	F39
Figure F.21 Comparison of J versus moment curves for a circumferential through-wall crack in a straight pipe and centered on the extrados of an elbow with an $R/t = 5$ and $2\theta=180$ degrees.....	F39
Figure F.22 Comparison of J versus moment ratios for a circumferential through-wall crack in a straight pipe and centered on the extrados of an elbow with an $R/t = 20$ and $2\theta=90$ degrees.....	F40
Figure F.23 Comparison of J versus moment ratios for a circumferential through-wall crack in a straight pipe and centered on the extrados of an elbow with an $R/t = 20$ and $2\theta=180$ degrees.....	F40
Figure F.24 Comparison of J versus moment ratios for a circumferential through-wall crack in a straight pipe and centered on the extrados of an elbow with an $R/t = 5$ and $2\theta=90$ degrees.....	F41
Figure F.25 Comparison of J versus moment ratios for a circumferential through-wall crack in a straight pipe and centered on the extrados of an elbow with an $R/t = 5$ and $2\theta=180$ degrees.....	F41
Figure F.26 Ratio of circumferentially through-wall-cracked pipe-to-elbow moments for constant applied J values versus the ASME B_2 index for the elbow.....	F42
Figure F.27 Comparison of J versus moment curves for an axial through-wall crack in a straight pipe and an axial through-wall crack on the flank of an elbow with an $R/t = 20$ and $2\theta=15$ degrees.....	F44
Figure F.28 Comparison of J versus moment curves for an axial through-wall crack in a straight pipe and an axial through-wall crack on the flank of an elbow with an $R/t = 20$ and $2\theta=30$ degrees.....	F44
Figure F.29 Comparison of J versus moment curves for an axial through-wall crack in a straight pipe and an axial through-wall crack on the flank of an elbow with an $R/t = 5$ and $2\theta=15$ degrees.....	F45
Figure F.30 Comparison of J versus moment curves for an axial through-wall crack in a straight pipe and an axial through-wall crack on the flank of an elbow with an $R/t = 5$ and $2\theta=30$ degrees.....	F45
Figure F.31 Comparison of J versus moment ratios for an axial through-wall crack in a straight pipe and an axial through-wall crack on the flank of an elbow with an $R/t = 20$ and $2\theta=15$ degrees.....	F46

Figure F.32 Comparison of J versus moment ratios for an axial through-wall crack in a straight pipe and an axial through-wall crack on the flank of an elbow with an $R/t = 20$ and $2\theta=30$ degrees.....	F46
Figure F.33 Comparison of J versus moment ratios for an axial through-wall crack in a straight pipe and an axial through-wall crack on the flank of an elbow with an $R/t = 5$ and $2\theta=15$ degrees.....	F47
Figure F.34 Comparison of J versus moment ratios for an axial through-wall crack in a straight pipe and an axial through-wall crack on the flank of an elbow with an $R/t = 5$ and $2\theta=30$ degrees.....	F47
Figure F.35 Ratio of axially through-wall-cracked pipe-to-elbow moments for constant applied J values versus the ASME B_2 index for the elbow.....	F48
Figure G.1 Geometry of VC Summer hot leg/RPV nozzle bimetallic weld joint.....	G3
Figure G.2 Piping system geometry.....	G4
Figure G.3 Photo of cold leg weld cross section (top) and computational weld model of cold leg.....	G6
Figure G.4 Welding process analysis flow chart for cold leg.....	G8
Figure G.5 Cold leg axis-symmetric cladding (buttering) and weld model.....	G9
Figure G.6 Weld process simulation.....	G10
Figure G.7a Temperature dependent true stress-strain curves of Inconel 182 tested by ORNL.....	G14
Figure G.7b Temperature dependent true stress-strain curves at A516 Grade 70.....	G15
Figure G.7c Temperature dependent true stress-strain curves of A508 Class 3 tested by ORNL.....	G15
Figure G.7d Temperature dependent true stress-strain curves of Type 316 and Type 309.....	G16
Figure G.7e Temperature dependent true stress-strain curves of Type 304.....	G16
Figure G.8 Axial stresses during heat treat process.....	G18
Figure G.9 Hoop stresses during heat treat process.....	G18
Figure G.10 Equivalent plastic strains.....	G19
Figure G.11 Equivalent creep strains.....	G19
Figure G.12 Residual stresses final (axial) at room temperature 22C (70°F).....	G20
Figure G.13 Residual stresses final (axial) at operating temperature 291°C (556°F).....	G20
Figure G.14 Residual stresses final (hoop) at room temperature 22°C (70°F).....	G21
Figure G.15 Residual stresses final (hoop) at operating temperature 291°C (556°F).....	G21
Figure G.16a Residual stresses final (axial) at operating temperature 291°C (556°F).....	G23
Figure G.16b Residual stresses final (axial) at operating temperature 291°C (556°F).....	G23

Figure G.16c Residual stresses final (hoop) at operating temperature 291°C (556°F).....	G24
Figure G.16d Residual stresses final (hoop) at operating temperature 291°C (556°F).....	G24
Figure G.17 Residual equivalent plastic strains in cold leg at room temperature	G25
Figure G.18 Residual axial (a), hoop (b), and shear (c), plastic strains in cold leg at room temperature	G26
Figure G.19 Geometry of V.C. Summer bi-metallic weld joint	G28
Figure G.20 Axis-symmetric model of V.C. Summer bimetallic weld joint.....	G28
Figure G.21 Welding process simulated on hot leg.....	G29
Figure G.22 Cladding (butter) and rejected weld model	G30
Figure G.23 Finite element analysis process flow.....	G31
Figure G.24 Full finite element model.....	G33
Figure G.25 Cladding simulation stresses (after cooling to room temperature).....	G33
Figure G.26 Cladding simulation – effective plastic strains.....	G34
Figure G.27 Post cladding heat treatment simulation – creep strains.....	G34
Figure G.28 Rejected weld and bridge simulation.....	G35
Figure G.29 Comparison of rejected weld and bridge simulation	G35
Figure G.30 Axial stress comparison between two sequences	G36
Figure G.31 Hoop stress comparison between two sequences	G36
Figure G.32 Effective plastic strain comparison between two sequences	G37
Figure G.33 Axial plastic strain comparison between two sequences.....	G37
Figure G.34 Hoop plastic strain comparison between two sequences.....	G38
Figure G.35 Shear plastic strain comparison between two sequences.....	G38
Figure G.36 Effect of hydro-test – axial stresses (pressure = 3.125 ksi, then unload)	G39
Figure G.37 Effect of hydro-test – hoop stresses (pressure = 3.125 ksi, then unload at room temperature).....	G40
Figure G.38 Axial residual stresses at operating temperature (after all welding and hydro-test) Top: room temperature before heat up to 324°C (615°F); Bottom: after heat up; left is for welding inside then outside, right is for welding outside then inside.....	G41
Figure G.39 Hoop residual stresses at operating temperature (after all welding and hydro-test) Top: room temperature before heat up to 324°C (615°F); Bottom: after heat up; left is for welding inside then outside; right is for welding outside then inside	G41
Figure G.40 Operation residual stresses (324°C (615°F) – no loading) for inside first weld (a) and (b). (c) and (d) mapped residual stresses at operating temperature from fine to coarse mesh. These stresses are then mapped to a three dimensional mesh (inside weld first, then outside weld).....	G42

Figure G.41 Operation residual stresses (324°C (615°F) – no loading) for outside first weld (a) and (b). (c) and (d) mapped residual stresses at operating temperature from fine to coarse mesh. These stresses are then mapped to a three dimensional mesh (outside weld first, then inside weld).....	G42
Figure G.42 Mapped hoop residual stresses at operating temperature from coarse axis-symmetric mesh to 3D mesh (inside weld first, then outside weld). (This 3D model is then used to obtain stress intensity factors via the finite element alternating method).....	G43
Figure G.43 Comparison of mapped hoop residual stresses at operating temperature from coarse axis-symmetric mesh to 3D mesh (inside weld first, then outside weld).....	G43
Figure G.44 Comparison of mapped hoop residual stresses at operating temperature from coarse axis-symmetric mesh to 3D mesh (outside weld first, then inside weld).....	G44
Figure G.45 Comparison of mapped equivalent plastic strains at operating temperature from coarse axis-symmetric mesh to 3D mesh (inside weld first, then outside weld).....	G44
Figure G.46 Normal operating loads applied on hot leg.....	G46
Figure G.47 Axial stresses – used for FEAM analyses: inside weld first then outside weld	G46
Figure G.48 Hoop stresses – used for FEAM analyses: inside weld first then outside weld	G47
Figure G.49 Axial stresses – used for FEAM analyses: outside weld first then inside weld	G47
Figure G.50 Hoop stresses – used for FEAM analyses: outside weld first then inside weld	G48
Figure G.51 Stress intensity factors; $a = 0.3, 0.4, 0.5$; $c/a = 1.5$. ‘NO LOAD’ = ‘Residual Stress Only’, ‘LOAD’ = ‘Residual Stress Plus Normal Operating Load’	G48
Figure G.52a Axial crack growth for the inside-out weld process	G50
Figure G.52b Approximation for the impact of the residual stress field on the crack size and shape.....	G50
Figure G.52c Three and six month crack growth shapes.....	G51
Figure G.53 Approximation for the impact of the residual stress field on the crack size and shape. The ‘red’ shape represents the crack shape for the case of loading and residual stresses (for the I-O case) and the ‘white’ shape is the crack shape for the residual stress only case after 6 months of PWSCC growth. The ‘red’ curve (I-O case) can be compared to the ‘gray’ (O-I case) curve for a comparison of the weld sequence effect.....	G51
Figure G.54a Circumferential PWSCC growth – inside weld first case.....	G52
Figure G.54b Circumferential PWSCC growth - outside weld first case.....	G52
Figure G.55a The impact of using a conservative PWSCC law on crack growth – axial crack.....	G53
Figure G.55b The impact of using a conservative PWSCC law on crack growth - circumferential crack.....	G53

Figure G.56 Hot leg 3D analysis geometry	G57
Figure G.57 Two-length and two-depth repair analyses.....	G57
Figure G.58 Weld directions.....	G58
Figure G.59 An example of the grinding and weld repair model during analysis.....	G58
Figure G.60 Baseline weld – axial stresses.....	G59
Figure G.61 Baseline weld – axial stresses.....	G59
Figure G.62 Baseline weld – Z-component stresses (these represent hoop stresses on the cut planes).....	G60
Figure G.63 Comparison of axial and hoop stresses between the axis-symmetric and 3D solutions.....	G60
Figure G.64 Comparison of axial stresses for repair case number 1	G61
Figure G.65 Comparison of axial stresses for repair case number 1	G61
Figure G.66 Repair L2 depth d1 – axial stresses	G62
Figure G.67 Repair L2 depth d1 – mean stress ($\sigma_{kk}/3$).....	G62
Figure G.68 Repair L2 depth d1 – axial stresses	G63
Figure G.69 Repair L2 depth D2 – mean stress ($\sigma_{kk}/3$).....	G63
Figure G.70 Repair L2 depth d2 – equivalent plastic strain	G64
Figure H.1 Typical axi-symmetric weld model construction	H4
Figure H.2 The thermal analysis showing weld build-up.....	H6
Figure H.3 Weld residual stress - axial stress.....	H7
Figure H.4 Weld residual stress -- hoop stress	H7
Figure H.5 Measured axial stress data versus analysis	H8
Figure H.6 Measured hoop stress data versus analysis.....	H8
Figure H.7 Model development - fine mesh - coarse mesh - 3-D mesh	H9
Figure H.8 Crack sizes.....	H9
Figure H.9 3-D crack mid-surface closed under zero load (top) and ready to open under critical tension loading (bottom).....	H9
Figure H.10 Crack OD opening profile under tension load, $\theta = \pi / 8$	H10
Figure H.11 GE/EPRI tension equation modification	H11
Figure H.12 Mesh density study results.....	H15
Figure H.13 Axial stress results from heat input study.....	H16
Figure H.14 Hoop stress results from heat input study.....	H16
Figure H.15 GE/EPRI bending equation modification.....	H18

Figure H.16 Comparison of results from combined loading example.....	H22
Figure H.17 Start -- Stop weld analysis model.....	H24
Figure H.18 Baseline weld -- axial stresses.....	H25
Figure H.19 Baseline weld -- axial stresses.....	H26
Figure H.20 Crack displacement results for $\pi /16$ crack in start-stop location and 180 degrees away from the start-stop location.....	H27
Figure H.21 Crack displacement results for $\pi /8$ crack in start-stop location and 180 degrees away from the start-stop location.....	H27
Figure H.22 Crack displacement results for $\pi /4$ crack in start-stop location and 180 degrees away from the start-stop location.....	H28
Figure H.23 Crack displacement results for $\pi /2$ crack in start-stop location and 180 degrees away from the start-stop location.....	H28
Figure H.24 Stress intensity factors for a surface crack growing through a residual stress field. Crack length, a_1 , remained constant while the crack depth, a_2 , increased (Taken from References H.7 and H.8).....	H32
Figure H.25 COD analysis including residual stresses and plastic strain history (thin lines) and only including residual stresses (denoted 'test').....	H33
Figure I.1 Photograph of fracture from aged cast stainless experiment (Experiment 1.3-7) from IPIRG-1	I2
Figure I.2 Net-Section-Collapse analyses predictions, with and without considering induced bending, as a function of the ratio of the through-wall crack length to pipe circumference	I3
Figure I.3 FE mesh used in past Battelle COD/Restraint effect study.....	I4
Figure I.4 Normalized graph showing the effects of restraining ovalization and rotations at different distances from the crack plane.....	I4
Figure I.5 Normalized COD versus restraint length for two different sets for FE analyses.....	I5
Figure I.6 Calculated maximum loads for LBB with and without restraint of the pressure- induced bending from the pipe system.....	I7
Figure I.7 Cracked-pipe geometry	I8
Figure I.8 Representative finite element mesh used by Participant A.....	I11
Figure I.9 Finite element mesh used by Participant B for symmetric restraint cases.....	I14
Figure I.10 Finite element mesh used by Participant B for asymmetric restraint cases	I14
Figure I.11 Boundary conditions for restraining the bending induced tension in the symmetric FE model.....	I15
Figure I.12 Boundary conditions for restraining the bending induced tension in the asymmetric FE model.....	I15
Figure I.13 The “Distributing Coupling Element” in ABAQUS.....	I16

Figure I.14 The finite element mesh and associated boundary conditions used by Participant C for the symmetric restraint cases	I16
Figure I.15 The finite element mesh and associated boundary conditions used by Participant C for the asymmetric restraint cases	I17
Figure I.16 Axial displacement and stress distributions using the distributing coupling element to impose the axial load (Case 1a, $L/D=1$, $\theta/\pi=1/8$, Participant C)	I17
Figure I.17 Boundary conditions and mesh used by Participant D.....	I18
Figure I.18 Typical finite element mesh for the symmetric case by Participant E.....	I19
Figure I.19 Typical finite element mesh for the asymmetric case by Participant E	I20
Figure I.20 Typical finite element mesh used by Participant F	I20
Figure I.21 Effect of pipe length on COD of unrestrained pipe for the longest crack length investigated in this program. Participant F	I22
Figure I.22 Comparison of the unrestrained COD values for Cases 1a-1c. The COD values are normalized with respect to the averaged COD value of all participants	I22
Figure I.23 Comparison of the unrestrained COD values from Participant C, E, and F for Cases 1a-1c. The COD values are normalized by the mean COD value of the three participants of the same case	I23
Figure I.24 Normalized COD values for Case 1a-1c from Participant A.....	I24
Figure I.25 Normalized COD values for Case 1a-1c from Participant C	I24
Figure I.26 Comparison of normalized COD in Case 1, half crack length = $\pi/8$	I25
Figure I.27 Comparison of normalized COD in Case 1, half crack length = $\pi/4$	I26
Figure I.28 Comparison of normalized COD in Case 1, half crack length = $\pi/2$	I26
Figure I.29 Comparison of normalized COD for all round-robin cases in Case 1, excluding the results from participant D and NUREG/CR-6443 (Ref. I.1).....	I27
Figure I.30 Effect of R_m/t ratio on normalized COD. Participant F, OD=28-inch	I28
Figure I.31 Effect of R_m/t ratio on normalized COD. Participant E, OD=28-inch.....	I28
Figure I.32 Effect of R_m/t ratio on normalized COD. Participant C, OD=28-inch.....	I29
Figure I.33 Effect of R_m/t ratio on normalized COD. Participant D, OD=28-inch	I29
Figure I.34 Normalized COD under asymmetric restraint length from Participant F	I31
Figure I.35 Normalized COD under asymmetric restraint length from Participant E.....	I31
Figure I.36 Normalized COD under asymmetric restraint length from Participant C.....	I32
Figure I.37 Pipe test analyzed in 1986 ASME PVP round robin.....	I33
Figure I.38 Results for 3D FE analysis of 1986 ASME PVP round robin - J versus load-line displacement	I34

Figure I.39 Results for 3D FE analysis of 1986 ASME PVP round robin - J values at initiation displacement versus number of nodes in ligament of FE model.....	I34
Figure I.40 Results for estimation analysis of 1986 ASME PVP round robin	I35
Figure I.41 Comparison of Brickstad and Miyoshi results showing good agreement between line-spring and very refined 3D FE results.....	I36
Figure I.42 Comparison of Mohan FE analyses of 1986 ASME PVP round-robin problem.....	I38
Figure I.43 Comparison of Mohan FE analyses of surface crack in an elbow	I38
Figure I.44 Differences in J -estimation scheme predictions for same diameter pipe crack dimensions of $\theta/\pi=0.5$ and $a/t=0.5$ and $n=5$	I40
Figure I.45 A typical model using shell and line-spring elements from Participant P1	I43
Figure I.46 Focused view of the shell and line-spring model, looking at the cross-sectional plane containing the line-spring elements.....	I43
Figure I.47 A typical 3-D solid element model from Participant P2.....	I44
Figure I.48 A focused view of the cracked region of a 3-D solid element model from Participant P2.....	I44
Figure I.49 The 3-D solid element model of Problem A-2 from Participant P3	I45
Figure I.50 The focused view of the flawed area of the 3-D solid element model for Problem A-2 from Participant P3.....	I46
Figure I.51 Application of bending and internal pressure by Participant P3.....	I47
Figure I.52 A deformed shell and line-spring model from Participant P1.....	I49
Figure I.53 Contours of axial stress of a deformed shell and line-spring model from Participant P1	I49
Figure I.54 The J versus moment relations of Case A-1. LS and LD stand for large strain and large displacement, respectively.....	I50
Figure I.55 The J versus moment relations of Case A-2	I50
Figure I.56 The J versus moment relations of Case A-3	I51
Figure I.57 The J versus moment relations of Case B-1.....	I52
Figure I.58 The J versus moment relations of Case B-2. SS and SD stand for small strain and small displacement, respectively.....	I52
Figure I.59 The J versus moment relations of Case C-1.....	I54
Figure I.60 The J versus moment relations of Case C-2.....	I54
Figure I.61 The J versus moment relations of Case C-3.....	I55
Figure I.62 Comparison of the line-spring results of Participant P1 with the 3-D solid element results of Anderson for a pipe section loaded in tension.....	I55

Figure I.63 Comparison of the 3-D solid element results of Participant P2 with the 3-D solid element results of Anderson for a pipe section loaded in tension	I56
Figure I.64 Comparison of the line-spring results of Participant P1 with the 3-D solid element results of Anderson for a pipe section loaded in bending.....	I56
Figure I.65 Comparison of the 3-D solid element results of Participant P2 with the 3-D solid element results of Anderson for a pipe section loaded in bending.....	I57
Figure I.66 Comparison of the normalized K solutions from the line-spring solution of Wang.....	I57

List of Tables

Table B.1 Test conditions for BINP Task 2 simulated seismic pipe-system experiment.....	B26
Table B.2 Test conditions for three stainless steel pipe-system experiments.....	B28
Table B.3 Test results from three stainless steel pipe-system experiments in terms of fracture ratios	B28
Table C.1 Plasticity validation analysis parameters	C6
Table C.2 Plasticity validation theoretical values for pure bending.....	C7
Table C.3 Plasticity validation deviation from theoretical values for pure bending	C8
Table C.4 Plasticity validation theoretical values for tension plus bending.....	C9
Table C.5 Plasticity validation deviation from theoretical values for tension plus bending	C10
Table C.6 IPIRG pipe loop system Actual Margins task cracks.....	C27
Table C.7 IPIRG pipe loop system Actual Margins runs	C29
Table C.8 IPIRG pipe system analysis margins.....	C33
Table D.1 Analysis matrix for symmetric restraint cases in round-robin FE calculations	D4
Table D.2 Analysis matrix for asymmetric restraint cases in round-robin FE calculations	D4
Table D.3 Additional Symmetric Cases used in Pipe Stiffness Analysis.....	D16
Table D.4 Dimensional and loading conditions for 18 critical locations considered in sample plant piping system test cases.....	D23
Table D.5 Comparison between restrained and unrestrained COD values.....	D24
Table E.1 Best-fit curve fitting coefficients and 15 percent conservative curve fitting coefficients for various crack locations and loading conditions	E3
Table E.2 Analysis matrix and dimensional and material parameters.....	E9
Table E.3 Surface regression coefficients.....	E29
Table E.4 Definition and equivalence of different transition temperature fracture parameters	E35

Table E.5 Circumferentially cracked A106B pipe test results and comparison to minimum temperature for ductile fracture	E50
Table E.6 Circumferentially cracked ferritic pipe test results and comparison to minimum temperature for ductile fracture	E51
Table E.7 Summary of the methodology and how the experimental data agreed with the anticipated transition temperatures for each specimen geometry	E61
Table F.1a Elbow with circumferential crack – combined pressure and bending compilation (R/t = 5, $\theta = 45^\circ$)	F24
Table F.1b Elbow with circumferential crack – combined pressure and bending compilation (R/t = 10, $\theta = 45^\circ$)	F24
Table F.1c Elbow with circumferential crack – combined pressure and bending compilation (R/t = 20, $\theta = 45^\circ$)	F25
Table F.2a Elbow with circumferential crack – combined pressure and bending compilation (R/t = 5, $\theta = 90^\circ$)	F26
Table F.2b Elbow with circumferential crack – combined pressure and bending compilation (R/t = 10, $\theta = 90^\circ$)	F26
Table F.2c Elbow with circumferential crack – combined pressure and bending compilation (R/t = 20, $\theta = 90^\circ$)	F27
Table F.3a Elbow with axial crack – combined pressure and bending compilation (R/t = 5, $\theta = 15^\circ$)	F28
Table F.3b Elbow with axial crack – combined pressure and bending compilation (R/t = 10, $\theta = 15^\circ$)	F29
Table F.3c Elbow with axial crack – combined pressure and bending compilation (R/t = 20, $\theta = 15^\circ$)	F30
Table F.4a Elbow with axial crack – combined pressure and bending compilation (R/t = 5, $\theta = 30^\circ$)	F31
Table F.4b Elbow with axial crack – combined pressure and bending compilation (R/t = 10, $\theta = 30^\circ$)	F32
Table F.4c Elbow with axial crack – combined pressure and bending compilation (R/t = 20, $\theta = 30^\circ$)	F33
Table F.5 Elbow with circumferential crack – pure bending compilation ($\theta = 45, 90^\circ$) for use with Equations E.19 and E.20 (a) R/t = 5, (b) R/t = 10, (c) R/t = 20	F34
Table F.6 Elbow with axial crack – pure bending compilation ($\theta = 15, 30^\circ$) for use with Equations E.19 and E.20 (a) R/t = 5, (b) R/t = 10, (c) R/t = 20	F35
Table G.1 Material properties for Inconel 182 weld material	G12

Table G.2	Temperature dependent material properties for A516-70.....	G12
Table G.3	Temperature dependent material properties for A508 Class 3	G13
Table G.4	Temperature dependent material properties for Type 316 and Type 309.....	G13
Table G.5	Temperature dependent material properties for Type 304.....	G14
Table G.6	Temperature dependent creep constants for all the materials.....	G17
Table H.1	Pipe geometries studied	H3
Table H.2	Crack sizes studied.....	H3
Table H.3	Energy inputs used in the current analysis.....	H5
Table H.3a	Energy inputs used in the current analysis.....	H5
Table H.4	Weld pass power input per unit volume for 0.590 inch thick pipe.....	H6
Table H.5	V_1 values for tension from Table 2-1 of Reference H.1	H10
Table H.6	V_1 values for bending from Table 2-5 of Reference H.1	H10
Table H.7	V_1 values for bending from Tables 4.3 and 4.8 of Reference H.6.....	H10
Table H.8	$\sigma^\infty_{\text{Critical}}$ values for tension loads kPa, (psi)	H11
Table H.9	C_1 values for tension (C_T).....	H12
Table H.10	I_{OD} values	H12
Table H.11	I_{ID} values	H13
Table H.12	C_1 values for moment loading (C_B)	H19
Table H.13	$\sigma^\infty_{\text{Critical}}$ values for moment loads kPa, (psi).....	H19
Table H.14	Combined loading example factors	H20
Table H.15	Calculated results for modified equation and GE / EPRI	H21
Table I.1	Differences in leakage flaw sizes due to restraint of pressure-induced bending.....	I6
Table I.2	Symmetric restraint cases.....	I8
Table I.3	Asymmetric restraint cases.....	I8
Table I.4	Problems analyzed by the participants	I9
Table I.5	Matrix of FE runs by Participant A – Case 1a.....	I12
Table I.6	Matrix of FE runs by Participant A – Case 1b	I12
Table I.7	Matrix of FE runs by Participant A – Case 1c.....	I13
Table I.8	Summary of model features.....	I21
Table I.9	Observations on unrestrained pipe case	I23
Table I.10	Observations on the round-robin case comparisons.....	I27

Table I.11	Normalized COD under asymmetric restraint length, OD=28-inch.....	I30
Table I.12	Normalized COD under asymmetric restraint length, OD=12.75-inch.....	I30
Table I.13	Normalized COD under asymmetric restraint length, OD=4.5-inch.....	I30
Table I.14	Post round-robin analyses of the 1986 ASME round-robin problem.....	I35
Table I.15	Initiation load predictions from IPIRG-1 round-robin using estimation schemes	I37
Table I.16	Maximum load predictions from IPIRG-1 round-robin using estimation schemes ..	I37
Table I.17	Summary of the problem sets and dimensional and material parameters	I42
Table I.18	Summary of the analysis procedures of all participants.....	I48

APPENDIX A

EVALUATION OF PROCEDURES FOR THE TREATMENT OF SECONDARY STRESSES IN PIPE FRACTURE ANALYSES

A.1 BACKGROUND

Currently, the flaw evaluation procedures embodied in ASME Section XI specify different safety factors for global secondary stresses, such as thermal expansion and seismic anchor motion (SAM) stresses, than they do for primary stresses, such as primary membrane or primary bending stresses. The ASME Code specifies a safety factor of 2.77 for Service Levels A and B, and 1.39 for Service Levels C and D for primary stresses. For cracks in ferritic materials (base metal and welds) and austenitic flux welds (submerge-arc and shielded-metal-arc welds), the Section XI procedures indicate that the thermal expansion stresses should be included, but with a safety factor of only 1.0. In addition, for cracks in austenitic base metals, the ASME Code indicates that thermal expansion stresses need not be considered. Furthermore, the current ASME Section XI procedures do not explicitly require SAM stresses to be considered, regardless of the material.

The R6 analysis classifies certain secondary stresses, such as thermal expansion and other displacement-induced stresses (SAM), as effectively being primary stresses if there is significant elastic follow-up at the crack section. These stresses will not generally be self-equilibrating as is typically assumed for secondary stresses, such as weld residual stresses.

In a similar view, the LBB procedures specified in draft Standard Review Plan (SRP) 3.6.3 have an option that allows the thermal expansion stresses to be considered in the stability analysis of cracks in austenitic submerge-arc and shielded-metal-arc welds, but not in the stability analysis of cracks in austenitic wrought base metals and TIG welds. For ferritic materials,

this option is not given so that secondary and primary stresses are combined.

A.2 RESULTS OF PRIOR PIPE-SYSTEM EXPERIMENTS

The results from the IPIRG pipe-system experiments indicate that for large cracks, where the failure stresses are below the general yield strength of the uncracked pipe, the thermal expansion and SAM stresses contributed just as much to fracture as did the primary stresses, see Figure A.1. Figure A.1 shows a plot of the maximum experimental stress normalized by the Net-Section-Collapse (NSC) stress for five quasi-static bend and five pipe-system experiments conducted as part of the IPIRG (Refs. A.1 and A.2) and related programs (Refs. A.3 and A.4). The crack sizes in each of these experiments were relatively large, such that the failure moments were low enough that plasticity was restricted to the crack section. The maximum experimental stresses have been normalized by the NSC stress to account for slight differences in pipe size and crack size. For each experiment, the maximum stress has been broken down into its various stress components, i.e., primary membrane, primary bending (inertial), seismic anchor motion, and thermal expansion (For the quasi-static bend companion experiments, the only stress components applicable are primary membrane and primary bending [quasi-static bending]). From Figure A.1 it can be seen that if the thermal expansion and SAM stresses are ignored in the stress terms for the pipe-system experiments, then the normalized failure stresses for the pipe-system experiments would only be 40 to 50 percent of normalized failure stresses for the quasi-static bend experiments. Consequently, it appears from these results that secondary stresses do contribute to fracture, at least for the case of large surface cracks where plasticity is limited.

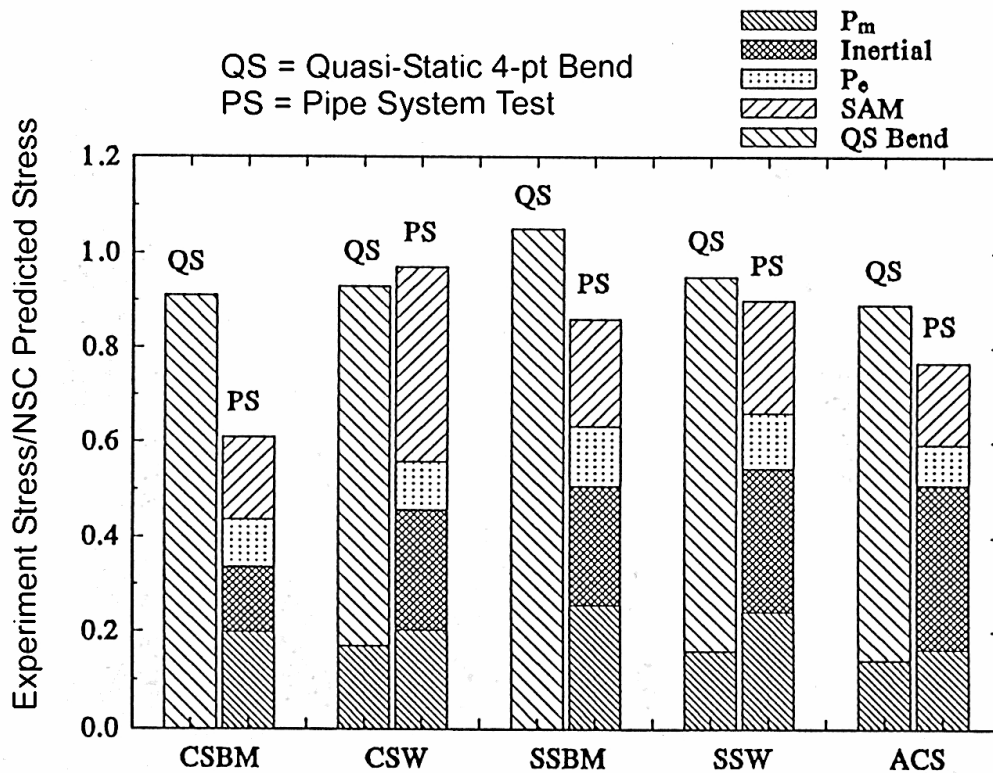


Figure A.1 Comparison of the results from the IPIRG-1 pipe-system experiments with companion quasi-static, four-point bend experiments demonstrating how global secondary stresses, such as thermal expansion and seismic anchor motion stresses, contribute to fracture

A.3 BINP TASK 1 EXPERIMENT

As part of this effort in the BINP program, another pipe-system experiment (BINP Experiment 1) was conducted. For this experiment the actuator was intentionally offset at the beginning of the experiment, prior to the application of the dynamic cyclic load history, to simulate a larger thermal expansion stress. Figure A.2 is a plot of the actuator time history for this experiment along with the actuator time history for its companion pipe-system experiment from the First IPIRG program, i.e., Experiment 1.3-5. The crack for both of these pipe-system experiments (1.3-5 from IPIRG-1

and BINP Experiment 1) was located in the center of a stainless steel submerge-arc weld. The crack sizes for both experiments were nominally the same, i.e., 50 percent of the pipe circumference in length and 66 percent of the pipe wall thickness in depth. From Figure A.2 it can be seen that the actuator for the BINP experiment was offset an additional 56 mm (2.2 inches) at the start of the experiment with respect to the actuator displacement for the IPIRG-1 experiment. This additional static offset in displacement resulted in an additional 255 kN-m (2,257 in-kips) of static moment at the crack section.

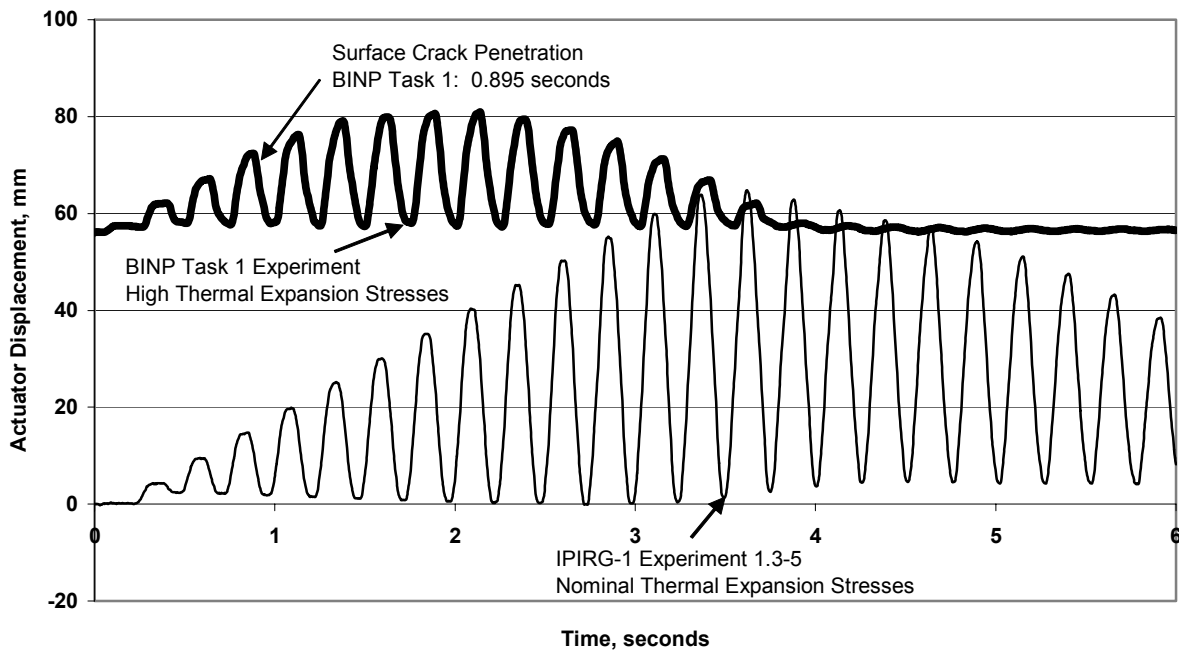


Figure A.2 Actuator time history for BINP Task 1 experiment and IPIRG-1 Experiment 1.3-5

Figure A.3 is a plot of the crack section moment as a function of time for these two pipe-system experiments up to the instant when the surface crack penetrated the pipe wall thickness. From this figure it can be seen that the total moment at the crack section at the instant of surface crack penetration was comparable for the two experiments. This further supports the contention that these global secondary stresses (thermal expansion and SAM stresses) contribute just as much to fracture as do the primary stresses, at least for the case where the

stresses in the uncracked pipe are below the yield strength of the pipe. From Figure A.4, which is a similar plot as Figure A.1, except it shows the results for the four stainless steel weld experiments (Experiment 4141-4 from the Degraded Piping Program, Experiment 1.3-5 from IPIRG-1, Experiment 1-5 from IPIRG-2, and the BINP Task 1 experiment), it can be seen that the primary stresses for the BINP Task 1 experiment represented only 35 percent of the total stress at maximum load.

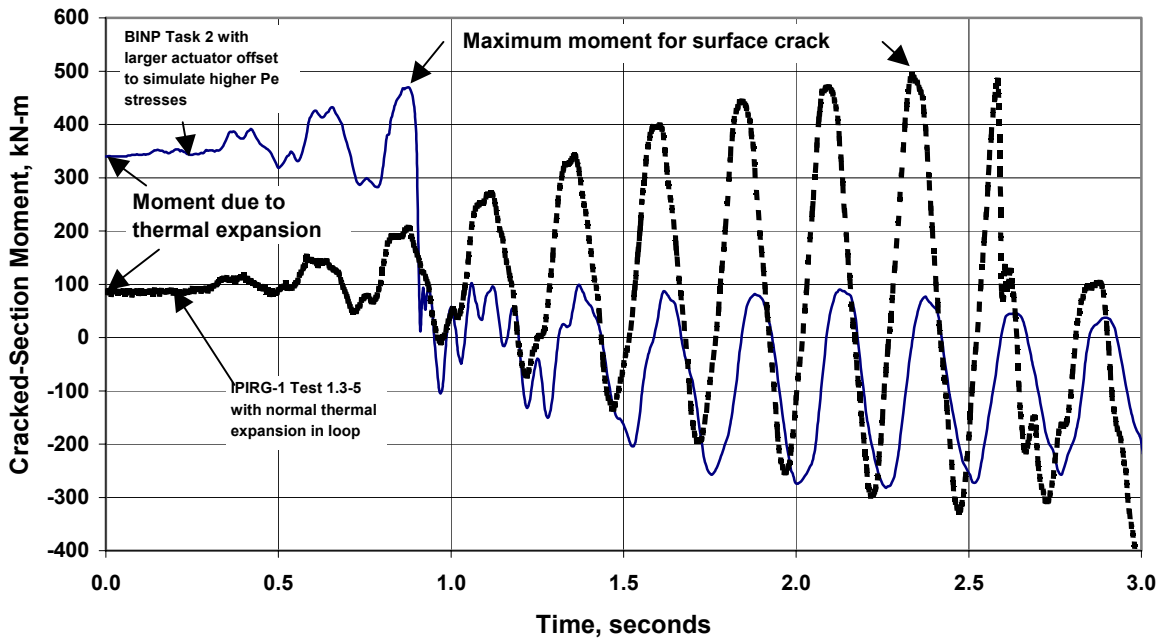


Figure A.3 Plot of crack section moment as function of time for BINP Task 1 experiment and IPIRG-1 Experiment 1.3-5

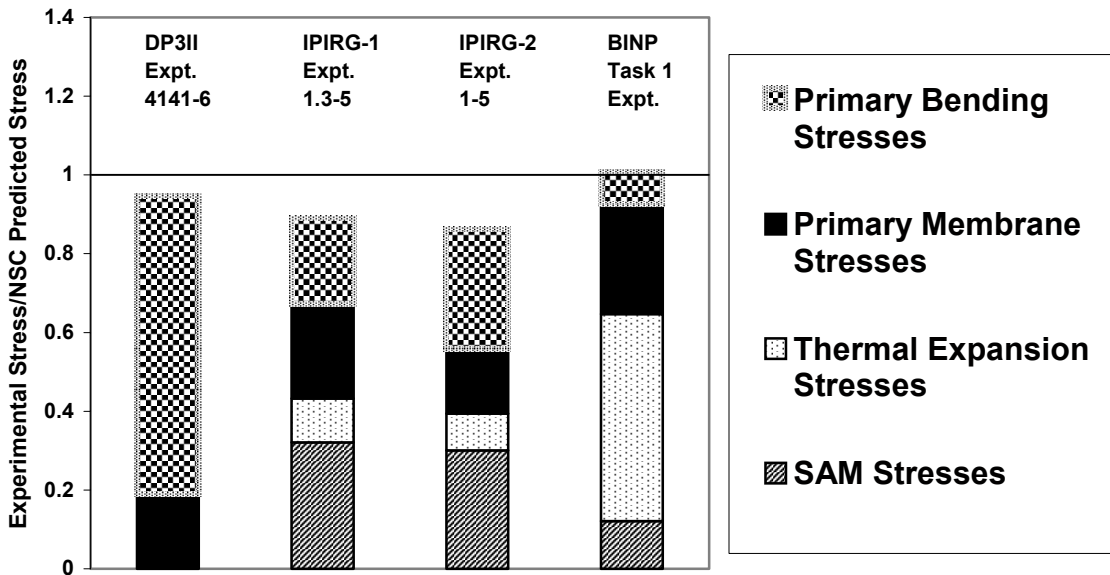


Figure A.4 Comparison of the results from four stainless steel weld experiments showing the contributions of the various stress components to pipe fracture

These findings support the contention that the thermal expansion and seismic anchor motion (SAM) stresses (secondary stresses) are as detrimental as the primary stresses, at least for these test conditions for which the stresses at failure for the uncracked pipe were less than the yield strength of the material.

For such conditions, there is the potential for elastic follow-up. Section III of the ASME code recognizes this potential in its local overstrain criteria in paragraph NC-3672.6(b). This paragraph implies that global secondary stresses, such as thermal expansion and seismic anchor motion stresses, can act as primary stresses under certain conditions, such as when the weaker or higher stressed portions of the piping system are subjected to strain concentrations due to elastic follow-up of the stiffer or lower stressed portions. One such obvious example of this is the IPIRG pipe system in which a large crack is introduced into a weaker material (lower yield strength) than the surrounding materials. Consequently, the resultant stresses for the uncracked pipe sections were less than the yield strength at the time of failure of the cracked section. The implication is that the safety margins for secondary stresses may be a function of the ratio of the failure stress to the yield strength. If the failure/yield stress ratio is less than 1.0, then global secondary stresses should probably be treated the same as primary stresses for fracture in the stability/critical crack size analyses. If the opposite holds true, then the global secondary stresses may become less important with some nonlinear function.

A.4 REFERENCES

A.1 Scott, P., Olson, R., and Wilkowski, G. Marschall, C., and Schmidt, R., "Crack Stability in a Representative Piping System Under Combined Inertial and Seismic/Dynamic Displacement-Controlled Stresses – Subtask 1.3 Final Report," NUREG/CR-6233, Vol. 3, June 1997.

A.2 Scott, P., Olson, R., Marschall, C., Rudland, D., Francini, R., Wolterman, R., Hopper, A., and Wilkowski, G., "IPIRG-2 Task 1 – Pipe System Experiments with

Circumferential Cracks in Straight-Pipe Locations," NUREG/CR-6389, February 1997.

A.3 Wilkowski, G., and others, "Degraded Piping Program – Phase II, Summary of Technical Results and Their Significance to Leak-Before-Break and In-Service Flaw Acceptance Criteria – March 1993 – December 1994," NUREG/CR-4599, Vol. 8, March 1989.

A.4 Kanninen, M., and others, "Instability Predictions for Circumferentially Cracked Type 304 Stainless Steel Pipes Under Dynamic Loadings," EPRI Report NP-2347, April 1982.